Author

Ryan Michael Gabelman

Title

Olivine-melt thermometry, hygrometry and oxybarometry applied to lavas erupted from the Mascota volcanic field, western Mexico

submitted in partial fulfillment of the requirements for the degree of
Master of Science in Earth and Environmental Sciences
Department of Earth and Environmental Sciences
The University of Michigan

Accepted by:

Rebecca Lange	Rebecca Lange	12/20/17
Signature	Name	Date
Gordon Moore	GORDON MOORE	12/20/17
Signature	Name	Date
Chris Poulsen	Chris Poulsen	12/22/17
Department Chair Signature	Name	Date

Earth and Environmental Sciences
UNIVERSITY OF MICHIGAN

Olivine-melt thermometry, hygrometry and oxybarometry applied to lavas erupted from the Mascota volcanic field, western Mexico

Ryan Michael Gabelman

Abstract

Olivine-melt thermometry, based on the partitioning of Ni, is applied to 13 lavas (absarokites, olivine minettes, basaltic andesites and a hornblende lamprophyre) from the Mascota volcanic field in western Mexico, to determine the onset temperature for olivine phenocryst growth during ascent. A test of whether the most Mg-rich olivine analyzed in each sample is a close approximation of the first olivine to crystallize from a melt composition that matches the whole rock was made using the thermodynamic MELTS model and shown to be consistent in all but one case. One sample with 16 wt% MgO, shows possible evidence of olivine accumulation, whereas the remaining 12 samples indicate that olivine crystallization began at ~1200 °C for the absarokites (~11.7 wt% MgO), ~1150 °C for the olivine minettes (~8.5 wt% MgO), ~1100-1030 °C for the basaltic andesites (~ 8.7-7.0 wt% MgO), and as low as ~954 °C for the hornblende lamprophyre. (~6 wt% MgO). These olivine-melt thermometry results are fully consistent with hydrous phase-equilibrium experiments from the literature. Moreover, all samples contain olivine phenocrysts with diffusion-limited rapid-growth textures, consistent with phenocryst growth driven by H_2O degassing and cooling during ascent, which leads to large effective undercoolings that cannot be attained in a magma undergoing cooling by conductive loss of heat in a crustal chamber. In addition to Ni-based olivine-melt thermometry, for which dissolved H_2O in the melt has a negligible

effect, the application of Mg-based olivine-melt thermometry to the same samples allows the magnitude of the suppression of olivine crystallization temperatures due to dissolved water in the melt to be evaluated. The results show that olivine liquidus temperatures have been reduced by 95-234 (± 29) °C, indicative of dissolved water concentrations that range from >3-8wt% H_2O, consistent with hydrous phase-equilibrium experiments. Finally, application of Fe^{2+}-Mg exchange coefficient (K_D) values from the literature to the olivine-melt pairs used for thermometry constrain melt Fe^{3+}/Fe^{T} ratios (0.25-0.49) at the onset of olivine growth; these values correspond to oxygen fugacities that range from 1 to 3 log units above that of the Ni-NiO buffer. The results of this study show that these 12 Mascota lavas, which display a strong arc geochemical signature (e.g., high Ba/Zr ratios) are both hydrous (≤ 8 wt%) and oxidized (ΔNNO ≤ +3).

Introduction

The Quaternary Mascota volcanic field in western Mexico has erupted a diverse suite of potassic magma types, such as olivine minettes, absarokites, and hornblende lamprophyres, together with calc-alkaline basaltic andesites and andesites. Previous studies have highlighted the enhanced arc geochemical signature of the minettes and lamprophyres, and suggested that they are further characterized by high oxidation states and water contents (e.g., Lange and Carmichael, 1991; Carmichael et al., 1996; Righter and Carmichael, 1996). However, existing estimates of oxidation states and water contents are only broadly constrained, with redox determinations from whole-rock ferric-ferrous analyses only (Carmichael et al., 1996) and only one sample (hornblende lamprophyre) has been successfully analyzed for water concentration through an olivine-hosted melt inclusion (~5 wt% H_2O, 1323 ppm CO_2; Maria and Luhr, 2008).

The primary objective of this study is to apply olivine-melt thermometry and oxybarometry to several olivine-bearing lavas, including absarokites, minettes, basaltic andesites, and hornblende lamprophyres, erupted from the Mascota volcanic field. Growing evidence shows that phenocryst growth in high-Mg basalts often occurs during ascent, and not in a stalled magma body within the crust, especially in samples erupted from small-volume, isolated cinder cones (e.g. Pu et al., 2017), which are common across the Mascota volcanic field. This allows the whole-rock composition of each sample to be used as a proxy for the melt composition, and the most Mg-rich olivine analyzed in each thin section to closely approximate the first olivine that crystallized at the liquidus. In this study, these two assumptions are tested through a comparison of the most Mg-rich olivine analyzed in each sample with the liquidus olivine compositions calculated for the whole-rock composition through the MELTS thermodynamic model (Ghiorso and Sack, 1995; Asimow and Ghiorso, 1998).

For samples that pass this test, two olivine-melt thermometers are applied, based on the partitioning of Mg ($D_{Mg}^{ol/liq}$) and Ni ($D_{Ni}^{ol/liq}$), respectively. Pu et al. (2017) shows that the Ni-based olivine-melt thermometer is largely independent of dissolved water content in the melt, unlike the Mg-based thermometer (e.g., Putirka et al., 2007). The difference in temperature between the two thermometers provides the magnitude of the depression of the olivine liquidus due to the effect of dissolved H_2O in the melt. This relationship yields a minimum water concentration in the melt at the onset of olivine phenocryst growth (Pu et al., 2017). These temperatures and water contents are compared to hydrous phase-equilibrium constraints from the literature on similar melt

compositions, as well as the H_2O concentrations measured in olivine-hosted melt inclusions from Mascota (Maria and Luhr 2008).

In addition to thermometery, it is also possible to use $^{Fe2+-Mg}K_D$ values between olivine and hydrous melt from the literature (Sisson and Grove, 1993a, 1993b; Wagner et al., 1995; Righter and Carmichael, 1996; Almeev et al., 2007; Medard and Grove, 2008; Parman et al., 2011), to constrain the melt ferric-ferrous ratio at the onset of olivine crystallization. These calculations allow for a test of whether lavas erupted from the Mascota volcanic field are systematically more oxidized than those erupted elsewhere in the Mexican arc.

Tectonic and Geological Setting

The Mascota volcanic field is located in the Jalisco tectonic block in western Mexico, where the Rivera Plate is actively subducting along the Middle America Trench (Fig. 1). Seismic studies constrain the depth of the Rivera Plate at ~140 km beneath the Mascota volcanic field (Yang et al., 2009). The Tepic-Zacoalco Rift to the north and the Colima Rift to the east (Luhr et al., 1985) both border the Jalisco block and are sites of active extension since at least ~5 Ma (e.g., Luhr et al., 1985; Rosas-Elguera et al., 1996; Ferrari and Rosas-Elguera, 2000; Frey et al., 2007).

The Rivera plate is a separated segment of the Farallon plate, which fragmented ~28 Ma when the Pacific-Farallon spreading ridge was overrode by North America. Subsequently, the Rivera and Cocos plates were separated between 8-5 Ma by a similar process (Lonsdale 1995). Seismic tomography shows a tear between the Rivera and Cocos plates, which has allowed hot asthenosphere to flow under the Jalisco block

lithosphere and may be driving partial melting of subduction-modified mantle lithosphere beneath the Mascota volcanic field (e.g., Ownby et al., 2008).

The volcanic field surrounding the towns of Mascota and San Sebastian (Figs 1 and 2) is comprised of ~87 small-volume cinder and lava cones (Ownby et al., 2008). All of the volcanic activity is contained within the N-S trending grabens, which are 2-5 km wide and up to 900 meters in relief (Carmichael et al., 1996). The basement of the Jalisco block is comprised of Cretaceous ash-flow tuffs, metamorphosed sediments and granitoid plutons (Wallace & Carmichael 1989; Lange & Carmichael, 1991; Carmichael et al., 1996; Frey et al., 2007).

The Mascota volcanic field is notable for the diversity of its lava types. Calc-alkaline basaltic andesites and andesites have erupted in close spatial and temporal association with potassic lavas including absarokites, olivine minettes, and hornblende-lamprophyres (Lange and Carmichael 1990; 1991; Carmichael et al., 1996; Maria and Luhr, 2008; Ownby et al., 2008). Notably, the Mascota volcanic field is the youngest of a series of volcanic fields within the Jalisco block with most erupted lavas erupted over the last 0.5 Ma (Carmichael et al., 1996; Ownby et al., 2008), and no age progression to the composition of magmas erupted. Ownby et al. (2008) used Arc GIS software and field maps to determine a total eruptive volume of 6.8±3.1 km^3, of which approximately half (3.5 ± 1.7 km^3) is potassic (absarokites, minettes and lamprophyres) and the other half (3.3 ± 1.4 km3) is calc-alkaline (basaltic andesites and andesites).

Previous work on intensive variables

Temperature

Previous efforts to constrain the temperature at which the Mascota lavas crystallized their phenocrysts are largely based on olivine-melt thermometry based on the partitioning of Mg (e.g., Lange and Carmichael, 1990; Maria and Luhr, 2008). However, it is now known that ($D_{Mg}^{ol/liq}$) depends strongly on the dissolved water concentration in the melt, and without including a correction for this effect, calculated temperatures are too high (e.g., Putirka et al., 2007). Other studies have compared the phenocryst assemblage in erupted lavas to hydrous phase-equilibrium experiments. This approach only provides broad constraints on temperature if a hydrous phenocryst such as phlogopite and/or hornblende is present. These two phases have maximum thermal stability limits that are documented for various melt compositions from hydrous phase-equilibrium experiments. For example, Righter and Carmichael (1996) performed experiments on an olivine minette with ~9.5 wt% MgO and showed that phlogopite is only stable at temperatures < 1150 °C. Thus, these Mg-rich magma must have crystallized at temperatures significantly below its 1-bar anhydrous liquidus (~1250 °C; Righter and Carmichael, 1996) under hydrous conditions. Similarly, Moore and Carmichael (1998) conducted experiments on a basaltic andesite with ~6.5 wt% MgO and showed that hornblende is only stable at temperatures < 1000 °C. The fact that none of the basaltic andesites from the Mascota volcanic field contain hornblende constrains their temperatures to be >1000 °C, whereas the hornblende lamprophyres with bulk compositions similar to basaltic andesites must have crystallized their hornblende phenocrysts at <1000 °C.

Water concentrations

The best constraint on dissolved water concentrations in magmatic melts at the time of phenocryst growth is from analysis of olivine-hosted melt inclusions. Only one melt-inclusion study has been performed on erupted magmas from the Mascota volcanic field. Maria and Luhr (2008) studied scoria from four cinder cones, of which three are included in this study (Mas-3, minette; Mas-21, basaltic andesite; Mas-9, hornblende lamprophyre). The fourth sample is another minette (Mas-4; Carmichael et al., 1996). Unfortunately, two of the four samples that Maria and Luhr (2008) studied had melt inclusions that were significantly degassed, with analyzed H_2O contents that ranged from 0.2-0.6 wt%. The basaltic andesite and hornblende lamprophyre samples (Mas-21 and Mas-9, this study) contain melt inclusions with up to 2.7 and 5.0 wt% H_2O, respectively. The hornblende lamprophyre additionally contains 1323 ppm CO_2 in the melt inclusion, whereas no CO_2 analyses are reported for any other sample (Maria and Luhr, 2008). These limited results illustrate the challenge in obtaining quantitative determinations of dissolved water contents in olivine-hosted melt inclusions, but also affirm the significantly high water contents required to suppress liquidus temperatures below the thermal stability limit of hornblende in lamprophyres with a bulk composition similar to basaltic andesites.

Oxygen fugacity

Unfortunately, ilmenite is not found in any of the lavas erupted from the Mascota volcanic field, although titanomagnetite is ubiquitous. The absence of ilmenite precludes the use of Fe-Ti oxide pairs to calculate temperature and oxygen fugacity in any of these samples. Therefore, previous studies have relied on whole-rock ferric-ferrous analyses of

unaltered Mascota lavas (i.e., no iddingsite rims on olivine) to infer that the potassic suite (absarokites, minettes and lamprophyres) is notably oxidized, with calculated oxygen fugacities up to 2-4 log units above the Ni-NiO buffer (Lange and Carmichael, 1991; Carmichael et al., 1996). Such high oxidation states are consistent with Fe^{3+}/Fe^{T} ratios of 0.77-0.87 in pristine phlogopite mineral separates from three Mascota minettes (Feldstein et al., 1996).

Another approach to constrain the oxidation state of basaltic andesites was used by Lange and Carmichael (1990). They showed that basaltic andesites from Mascota contained olivine phenocrysts that ranged to higher Fo contents relative to olivines in similar basaltic andesites (similar MgO and FeO^{T} wt%) erupted in the central Mexican arc. Their hypothesis was that the Mascota basaltic andesites had higher Fe^{3+}/Fe^{T} ratios, leaving less Fe^{2+} available for olivine. Thus, their argument was qualitative, but used to suggest that the basaltic andesites erupted in close association with the potassic suite were more oxidized than magmas erupted elsewhere in the Mexican arc.

Whole-Rock Geochemistry

Rock samples used in this study were obtained from the collection of Lange and Carmichael (1990, 1991) and Carmichael et al. (1996). Major element concentrations were obtained by wet chemical analysis performed by I.S.E Carmichael, with trace elements determined by X-ray fluorescence spectrometry (Table 1). To cover the wide range of lava types found within the Mascota volcanic field, 13 samples were targeted for this study: three absarokites, three olivine minettes, one hornblende-lamprophyre, and six basaltic andesites. The absarokites range from ~48-50% wt.% SiO_2, contain phenocrysts

of olivine, and augite, and lack phlogopite, hornblende, and plagioclase (Carmichael et al., 1996). The olivine minettes range from 49-52% wt.% SiO_2, with phenocrysts of olivine, augite, and phlogopite, and no plagioclase or hornblende (Lange & Carmichael, 1990; Carmichael et al., 1996). The hornblende lamprophyre has 52 wt.% SiO_2 and contains phenocrysts of olivine, augite, hornblende, and phlogopite (Carmichael et al., 1996). The basaltic andesites range from 52-56 wt.% SiO_2, with a phenocryst assemblage of olivine ± plagioclase ± augite, and no phlogopite or hornblende present (Lange & Carmichael 1990).

Olivine Compositions

Methods

Thirteen new thin sections were prepared from the 13 samples in Table 1. The compositions of olivine phenocrysts in these thin sections were analyzed using a Cameca SX100 electron microprobe. A focused beam with an accelerating voltage of 15 kV and a current of 20 nA was used. Eight elements (Mg, Al, Si, Ca, Cr, Mn, Fe, and Ni) were analyzed on 5 spectrometers, with peak and background counting times set at 20 s. For each sample, 15-25 olivine phenocrysts were analyzed. Each olivine was analyzed on a traverse line, with approximately 30-μm spacing between points. This resulted in 20-80 analyses per olivine crystal, and a range of 92-748 analyses per sample. A filter was applied to the data, where only analyses with totals of 99-100.9 were used.

Results

All olivine analyses for each sample are provided in Appendix Table 1. Results are summarized for each sample in histograms of olivine composition (Fo mol%; Fig. 3),

which show no break in composition up to the most Fo-rich olivine analyzed in each sample (Table 2). There is no evidence of bimodal and/or skewed distributions, which might be indicative of xenocrysts. A plot of NiO (wt%) in olivine as a function of Fo content (mol%) is shown in Figure 4 for each sample. A linear fit to the data for the top 3 mol% Fo olivines allows the NiO content to be calculated for the most Fo-rich olivine in each sample.

Conditions of Phenocryst Growth

Application of the Ni-olivine thermometer, where the whole-rock composition of each sample represents the liquid composition at the onset of olivine crystallization, depends on whether or not phenocryst growth occurred slowly in a crustal magma chamber or rapidly during ascent (Figure 5). Only in the second scenario can the assumption be made that the most Mg-rich olivine analyzed in each sample closely approximates the composition of the first olivine to crystallize from a melt with a composition close to that of the whole rock. The MELTs thermodynamic model (Ghiroso and Sack 1995; Asimow and Ghiorso, 1998) can be used to test the viability of this assumption.

In Figure 6, the most Mg-rich olivine analyzed in each sample is compared to the composition calculated by MELTS for the first olivine to crystallize from a melt with the whole-rock composition of that sample. The MELTS calculations are run at four different oxidations states (different melt ferric-ferrous ratios, which affects the liquidus olivine composition) to evaluate if there is a match between observed and calculated olivine compositions at reasonable oxidation states. The results (Fig. 6) show that most of

the Mascota suite could have crystallized their olivine phenocrysts during ascent at oxygen fugacities that are 1-2 log units above that for the quartz-fayalite-magnetite buffer (ΔQFM = +1 to +2).

A second test of rapid phenocryst growth of olivine during ascent is based on back-scattered electron (BSE) images (Fig. 7). There is ample evidence that many olivine phenocrysts in each sample exhibit diffusion-limited rapid growth textures. These textures develop when melts undergo large effective undercoolings ($\Delta T_{eff} = T_{Liquidus} - T_{Melt}$) (Lofgren 1974). Hopper textures observed are consistent with those produced during undercoolings caused by rapid H_2O degassing and/or cooling during magma ascent (Welsch et al. 2014; Waters et al. 2015).

Olivine-Melt Thermometry

The partitioning of both Mg and Ni between olivine and melt is known to vary strongly with temperature (e.g., Beattie, 1993; Li and Ripley, 2010), and therefore values of $D_{Mg}^{oliv/liq}$ and $D_{Ni}^{oliv/liq}$ can be used as a thermometer. Pu et al. (2017) demonstrate that both Mg- and Ni-based olivine-melt thermometers perform equally well at 1 bar over a wide range of anhydrous melt compositions and temperatures, with a 1σ error on T_{Mg} and T_{Ni} of $\pm$ 26 and 29 °C, respectively. The critical limitation of olivine-melt thermometers based on $D_{Mg}^{oliv/liq}$ is its sensitivity to dissolved H_2O in the melt (Putirka et al., 2007). Therefore, all olivine-melt thermometers based on the partitioning of Mg require a correction for H_2O (e.g., Putirka et al., 2007). In the absence of any H_2O correction, temperatures calculated from the Mg-based thermometer (T_{Mg}) represent anhydrous temperatures.

The basis of the Pu et al., (2017) Ni-based thermometer is found in Li and Ripley's (2010) model to investigate the temperature dependence of $D_{Ni}^{oliv/liq}$ in mantle partial melts. $D_{Ni}^{oliv/liq}$ is then exploited to yield olivine liquidus temperatures, T_{Ni}. The nickel content used in the Pu et al., (2017) model is calculated using the most forsteritic olivine observed and the linear relationship established between NiO wt% and Fo mol% (Figure 4). This nickel content is then combined with nickel content in the whole rock to calculate $D_{Ni}^{oliv/liq}$ at the onset of olivine crystallization. T_{Ni} is largely insensitive to dissolved H_2O content, and therefore represents the actual onset temperature for olivine crystallization at the liquidus, irrespective of the concentration of water in the melt (Pu et al., 2017).

Table 1 summarizes the olivine-liquidus temperatures (T_{Ni}) calculated for each sample. Temperatures range from 1218-1193 ºC for the absarokites, 1152-1088 °C for the olivine minettes, 1102-1033 °C, for the basaltic andesites, and 954 °C for the hornblende lamprophyre.

Olivine-Melt Hygrometry

A direct comparison between T_{Ni} and T_{Mg} provides an approximation of how much the liquidus temperature has been depressed due to dissolved H_2O in the melt. Dissolved H_2O in magmas lowers the olivine liquidus temperature, leading to positive values for ΔT ($=T_{Mg} - T_{Ni}$) in hydrous basalts (Almeev et al., 2007; Medard and Grove 2008; Pu et al., 2017). Moreover, the magnitude of ΔT scales with the concentration of dissolved H_2O in the melt. This relationship provides an opportunity to place broad constraints on minimum melt water concentration as a function of ΔT on the basis of

numerous hydrous olivine-melt equilibrium experiments in the literature. This calibration was performed in Pu et al. (2017) and is used in this study to estimate minimum concentrations of dissolved water in each sample at the onset of olivine crystallization. ΔT values and associated minimum wt% H_2O values are summarized in Table 1. The suppression of the olivine liquidus temperature ranges from ~96-210 °C in the absarokites, ~112-139 °C in the olivine minettes, ~109-207 °C in the basaltic andesites, and ~234 °C in the hornblende lamprophyre. The average of these ΔT (= T_{Mg} - T_{Ni}) values is 150 °C, which correlates to a minimum H_2O content in the melt of ~5.4 wt% at the onset of olivine crystallization.

Olivine-Melt Oxybarometry

To establish an effective oxybarometer based on olivine-melt equilibrium at the liquidus, Pu et al., (2017) examined $^{Fe2+-Mg}K_D$ values from a large number of hydrous phase-equilibrium experiments on basalts. A pool of 108 basalt liquid-olivine experiments from eight separate studies (Sisson and Grove, 1993a, 1993b; Wagner et al., 1995; Righter and Carmichael, 1996; Almeev et al., 2007; Medard and Grove, 2008; Parman et al., 2011) yielded an average $^{Fe2+-Mg}K_D$ of .37 ± .04 (Pu et al., 2017). This value is large than the value for $^{Fe2+-Mg}K_D$ of .34 presented in Matzen et al., (2011) on the basis of 446 anhydrous 1-bar olivine-melt experiments from the literature. Pu et al. (2017) shows that the $^{Fe2+-Mg}K_D$ between olivine and melt may be influenced by dissolved H_2O content because hydroxyl groups preferentially bond with Mg^{2+} relative to Fe^{2+} in the melt (e.g., Waters and Lange, 2017). Given the evidence that the Mascota magmas

contained significant amounts of dissolved water, with relatively large ΔT (= T_{Mg} - T_{Ni}) values, the average $^{Fe2+-Mg}K_D$ of .37 from Pu et al. (2017) is used in this study.

Application of this K_D value allows the melt Fe^{2+} concentration to be calculated, and when combined with the concentration of total iron, melt Fe^{3+}/Fe^T ratios can be calculated. The results are tabulated for all samples in Table 1 and show that all but two samples have Fe^{3+}/Fe^T ratios that range from 0.25-0.49. With melt ferric-ferrous ratios in hand, together with temperature (T_{Ni}) and whole-rock composition, an fO_2 relative to the Ni-NiO buffer can be calculated through the calibrated model equation provided in Jayasuriya et al., (2004). In Table 1, all calculated ΔNNO values (=logfO_2[sample] – logfO_2[Ni-NiO buffer]) are shown. With the exception of two absarokites, ΔNNO values range from +1 to +3. In contrast, two absarokites have low Fe^{3+}/Fe^T ratios and low ΔNNO values, which may be indicative of either olivine accumulation or low oxidation states.

Discussion

Consistency with hydrous phase-equilibrium experiments

A test of the results obtained from the new Ni-based olivine-melt thermometer, which is largely independent of melt water concentration, to the Mascota suite of lavas can be made for those samples for which there are hydrous phase-equilibrium experiments published on similar melt compositions. For example, Moore and Carmichael (1998) published a phase diagram for a basaltic andesite (Mas-22; Fig. 8) with a composition that is broadly similar to that for one of the basaltic andesites (Mas-19) and the hornblende lamprophyre (Mas-9). In Figure 8, a simplified plot of the phase stability fields for olivine, plagioclase, and hornblende are shown on a plot of P_{H2O} vs.

temperature based on the results of Moore and Carmichael (1998). Also shown are isopleths of melt H_2O concentration based on the H_2O solubility model of Zhange et al. (2007). The calculated temperature for Mas-19 at the onset of olivine crystallization is 1072 (± 29) °C, which is projected onto the phase diagram in Figure 8 and shows that the melt contained ~5 wt% H_2O at the olivine liquidus for that temperature. The hypothesis that Mas-19 crystallized its olivine phenocrysts during ascent is fully consistent with the hydrous phase-equilibrium experiments of Moore and Carmichael (1998) as well as the diffusion-limited growth textures for olivine in that sample (Fig. 6).

The hydrous phase diagram shown in Figure 8 can also be applied to the results for Mas-9, which is a hornblende lamprophyre with a bulk composition broadly similar to that for Mas-22 (similar wt% MgO). The experiments of Moore and Carmichael (1998) did not exceed P_{H2O} values of 303 MPa, and therefore the dT/dP_{H2O} slopes of the olivine and hornblende stability fields are extrapolated up to 500 MPa (Fig. 8). Nonetheless, the Ni-based olivine-melt temperature calculated for Mas-9 at the onset of olivine crystallization is 954 (± 29) °C, which is well within the hornblende stability field documented by Moore and Carmichael (1998). Therefore, the hypothesis that Mas-9 grew its phenocrysts during ascent is fully consistent with the phase diagram in Figure 8. Moreover, the evidence is consistent with Mas-9 containing much more dissolved water (> 8 wt%) at the onset of olivine crystallization relative to the case for Mas-19, which matches their respective ΔT (T_{Mg}-T_{Ni}) values (Table 1). These results are also consistent with the water analyses of 5 wt% in olivine-hosted melt inclusion (Maria and Luhr, 2008); it is fully expected that water contents in trapped melt inclusions will be lower than those at the liquidus, because full entrapment of the melt inclusion requires

continued olivine crystallization. It is well understood that analyses of olivine-hosted melt inclusions only provide minimum constraints on the water concentrations in the melt at the onset of olivine crystallization.

Another set of comparisons can be made utilizing the hydrous phase-equilibrium experiments of Righter and Carmichael (1996) on an olivine minette, with a bulk composition broadly similar to that for Mas-3 and Mas-11 in this study. The T_{Ni} values obtained for both of these samples, marking the onset of olivine crystallization, are 1152 and 1140 (± 29°C), respectively. These temperatures are consistent with the thermal stability limit of phlogopite (< 1180 °C) established through the experiments Righter and Carmichael (1996). The average of these two temperatures (1146 °C) crosses the olivine-in curve in the hydrous experiments of Righter and Carmichael (1996) at a P_{H2O} of ~160 MPa, which leads to a water concentration in the melt of ~5 wt%, based on the water solubility model of Zhang et al. (2007). Again, the results for Mas-3 and Mas-11 obtained from this study, based on the assumption of phenocryst growth during ascent, are fully consistent with the phase-diagram produced by Righter and Carmichael (1996).

Comparison of results from the Mascota suite with those for calc-alkaline lavas from the central Mexican arc

In previous petrological studies of the Mascota volcanic field (e.g., Lange and Carmichael, 1990, 1991; Carmichael et al., 1996), it was inferred that the potassic magmas (lamprophyres, minettes, absarokites) were notably more oxidized and hydrous than the calc-alkaline magmas (basalts and basaltic andesites), which in turn were more oxidized and hydrous than similar calc-alkaline basalts and basaltic andesites erupted in

the central Mexican arc (the Michoacán-Guanajuato volcanic field; Fig. 1). The results from this study show that there is considerable overlap in the calculated ΔT ($= T_{Mg} - T_{Ni}$) results (proxy for melt water concentration) for the potassic vs. calc-alkaline suite in the Mascota volcanic field.

The highest ΔT values (>200 °C) include two basaltic andesites, one absarokite, and the one hornblende lamprophyre; only two of these four samples are characterized by high Fe^{3+}/Fe^{T} ratios (≥ 40). Of the two with low Fe^{3+}/Fe^{T} ratios (≤ 20), one of these is LV-134, which contains 16 wt% MgO, and is characterized by an extremely low Fe^{3+}/Fe^{T} ratio, despite a calculated ΔT value of 211 °C. One possibility for this sample is that it is formed due a relatively large degree of melting of a mantle source that was dominated by relatively depleted (and possibly reduced) harzburgite wall rock, and a relatively small involvement of a hydrous vein component. Another possibility is that this sample is characterized by accumulation of significant amounts of olivine, leading to such a high MgO concentration (16 wt%). Additional analyses of other phases in this sample, including ferric-ferrous measurements of clinopyroxene phenocrysts, are needed to further evaluate these competing hypotheses. The second sample is Mas-149, a basaltic andesite, for which only 92 analyses of olivine were obtained. The histogram of olivine compositions shows a high abundance of the most Mg-rich olivine population, which is not expected given the abundance of olivine that crystallizes at the liquidus should be relatively low. This result suggests that additional olivine analyses are needed on multiple thin sections of Mas-149 to firmly establish the most Mg-rich olivine composition for this sample. The remaining Mascota samples show a broad correlation

between ΔT and melt Fe^{3+}/Fe^{T} ratios, which is consistent with slab-derived H_2O-rich fluid as the oxidizing agent, as proposed by Carmichael et al. (1991, 1996).

Another comparison can be made between the basaltic andesites from Mascota (this study) and those from the Michoacán-Guanajuato volcanic field (Pu et al., 2017). In Figure 9, histograms of ΔT and Fe^{3+}/Fe^{T} are shown that compare the two suites. The results show overlap, but an extension to higher ΔT and Fe^{3+}/Fe^{T} values for the Mascota basaltic andesites. More data are needed to fully establish whether there the Mascota suite is systematically more hydrous and oxidized than calc-alkaline lavas erupted elsewhere in the arc. Based on the results obtained in this study, the average ΔT and average Fe^{3+}/Fe^{T} are higher for the Mascota suite relative to those in the Michoacán-Guanajuato volcanic field, but there is significant overlap.

Conditions of phenocryst growth in the Mascota suite

Critical to the efficacy of this study is that the analyzed olivine phenocrysts grew during ascent and not in a stalled magma chamber. The evidence presented in this study shows that this remains a viable hypothesis for at least 12 of 13 samples. Phenocryst growth during magmatic ascent is consistent with the observed diffusion-limited growth textures of olivine phenocrysts in all the samples. Diffusion-limited growth textures are difficult to produce in stalled magma chambers undergoing slow cooling and crystallization and the absence of any undercoolings (Lofgren 1974; Waters et al., 2015). More commonly, these rapid-growth textures occur due to the large effective undercoolings that develop during ascent because of rapid H_2O degassing and/or cooling (Welsch et al. 2014; Waters et al. 2015).

The geomorphology of the Mascota volcanic field also suggests the absence of large, stalled chambers as the source of the eruptions. Over 87 small-volume cinder cones and associated lava flows over an area of ~2000 km^2 have an estimated total erupted volume of 6.8 ±3.1 km^3. The average erupted volume per vent is < 0.1 km^3 (Ownby et al., 2008). The combination of such low erupted volumes, and the scattered nature of the isolated vents, is fully consistent with the absence of stalled basaltic magmas in the upper crust. It is this characteristic, phenocryst growth during ascent, which enables olivine-melt thermometry, hygrometry, and oxybarometry to be applied to these samples.

Conclusions

The unique petrologic diversity of Quaternary magmas erupted in the Mascota volcanic field leads to considerable interest in obtaining information on the temperatures, dissolved water concentrations, and oxidation states of these melts at the onset of phenocryst growth. Traditional Mg-based olivine-melt thermometers are highly sensitive to dissolved melt water contents. Their application, therefore, is problematic in the Mascota volcanic field, where there is abundant evidence (i.e., the occurrence of hydrous phenocrysts) that dissolved water contents were high. A thermometer that is insensitive to water content (Ni-based olivine-melt thermometer; Pu et al., 2017) and accurately estimates the onset temperature of olivine crystallization at the liquidus leads to results that are consistent with hydrous phase-equilibrium experiments in the literature (e.g. Righter and Carmichael 1996; Moore and Carmichael 1998).

The Ni-based olivine-melt thermometer produces systematically lower temperatures when compared to results form the Mg-based olivine-melt thermometer.

Resulting ΔT ($T_{Mg} - T_{Ni}$) values for the Mascota suite range from 95-234ºC (±29ºC), with an average of 150 °C, indicative of high melt water concentrations at the onset of olivine crystallization (average of ~5 wt%). Inferred melt Fe^{3+}/Fe^{T} ratios, based on a Fe2+-Mg exchange coefficient of 0.37 (Pu et al., 2017), leads to ΔNNO values that largely cluster between +1 to +3. These results suggest that the oxidation state of the Mascota suite is systematically higher than most arc magmas (ΔNNO = ~0), but not as high (ΔNNO ≤ 4) as inferred by Lange and Carmichael (1991) and Carmichael et al. (1996) on the basis of whole-rock ferric-ferrous measurements.

Finally, there is no evidence to support a stalled magma chamber as a source of the eruptions in the Mascota volcanic field. The hypothesis that the phenocrysts in the erupted lavas largely grew during ascent remains viable.

References

Almeev, R.A., Holtz, F., Koepke, J., Parat, F., Botcharnikov, R.E. (2007) The effect of H_2O on olivine crystallization in MORB: experimental calibration at 200 MPa. American Mineralogist, 92, 670-674.

Asimow, P.D. and Ghiorso, M.S. (1998) Algorithmic modifications extending MELTS to calculate subsolidus phase relations. American Mineralogist, 83, 1127-1131.

Asimow, P.D., Hirschmann, M.M., Stolper, E.M. (2001). Calculation of peridotite partial melting from thermodynamic models of minerals and melts, IV. Adiabatic decompression and the composition and mean properties of mid-ocean ridge basalts. Journal of Petrology, 42, 963-998.

Beattie, P. (1993) Olivine-melt and orthopyroxene-melt equilibria. Contributions to Mineralogy and Petrology, 115, 103-111.

Carmichael, I.S.E. (1991) The redox states of basic and silicic magmas: a reflection of their source regions? Contributions to Mineralogy and Petrology, 106, 129-141.

Carmichael, I.S.E., Lange, R.A., and Luhr, J.F. (1996) Quaternary minettes and associated volcanic rocks of Mascota, western Mexico: a consequence of plate extension above a subduction modified mantle wedge. Contributions to Mineralogy and Petrology, 124, 302-333.

Feldstein, S.N., Lange, R.A., O'Neil, J.R. (1996) Ferric-ferrous ratios, H_2O contents and D/H ratios of phlogopite and biotite from lavas of different tectonic regimes. Contributions to Mineralogy and Petrology, 126, 51-66.

Ferrari, L., Rosas-Elguera, J. (2000) Late Miocene to Quaternary extension at the northern boundary of the Jalisco block, western Mexico: In: Delgago-Granados, H., Aguirre-Díaz, G.J., Stock, J.M. (Eds.) Cenozoic Tectonics and Volcanism of Mexico: the Tepic-Zacoalco Rift Revisited. Geological Society of America Special Paper, vol. 334, pp. 41-64.

Frey, H.M., Lange, R.A., Hall, C.M., Delgado-Granados, H. Carmichael, I.S.E. (2007) A Pliocene ignimbrite flare-up along the Tepic-Zacoalco rift: Evidence for the initial stages of rifting between the Jalisco Block (Mexico) and North America. Geological Society of America Bulletin, 119, 49-64.

Ghiorso, M.S. and Sack, R.O. (1995) Chemical mass-transfer in magmatic processes 4. A revised and internally consistent thermodynamic model for the interpolation and extrapotion of liquid-solid equilibria in magmatic systems at elevated temperatures and pressures. Contributions to Mineralogy and Petrology, 119, 197-212.

Jayasuriya, K. D., O'Neill, H. St. C., Berry, A. J., Campbell, S. J. (2004) A Mössbauer study of the oxidation state of Fe in silicate melts. American Mineralogist, 89, 1597-1609.

Lange, R.A. and Carmichael, I.S.E. (1990) Hydrous basaltic andesites associated with minette and related lavas in western Mexico. Journal of Petrology, 31, 1225-1259.

Lange, R.A. and Carmichael, I.S.E. (1991) A potassic volcanic front in western Mexico: the lamprophyric and related lavas of San Sebastian. Geological Society of America Bulletin, 103, 928-940.

Maria, A.H. and Luhr, J.F. (2008) Lamprophyres, basanites, and basalts of the western Mexican volcanic belt: volatiles and a vein-wallrock melting relationship. Journal of Petrology, 49, 2123-2156.

Li, C. and Ripley, E.M. (2010) The relative effects of composition and temperature on olivine-liquid Ni partitioning: statistical deconvolution and implications for petrologic modeling. Chemical Geology, 275, 99–104.

Lofgren, G. (1974) An experimental study of plagioclase crystal morphology: isothermal crystallization. American Journal of Science, 274, 243-273.

Lonsdale, P. (1995) Segmentation and disruption of the East Pacific Rise in the mouth of the Gulf of California. Marine Geophysical Research, 17, 323-359.

Luhr, J.F., Nelson, S.A., Allan, J.F. and Carmichael, I.S.E. (1985) Active rifting in southwestern Mexico: manifestations of an incipient eastward spreading ridge jump. Geology, 13, 54-57.

Matzen, A. K., Baker, M. B., Beckett, J. R., Stolper, E. M. (2011) Fe-Mg partitioning between olivine and high-magnesian melts and the nature of Hawaiian parental liquids. Journal of Petrology, 52,1243-1263.

Médard, E. and Grove, T.L. (2008) The effect of H_2O on the olivine liquidus of basaltic melts: experiments and thermodynamic models. Contributions to Mineralogist and Petrologist, 155, 417-432.

Moore, G. and Carmichael, I.S.E. (1998) The hydrous phase equilibria (to 3 kbar) of an andesite and basaltic andesite from western Mexico: constraints on water content and conditions of phenocryst growth. Contributions to Mineralogist and Petrologist, 130:304-319.

Ownby, S.E., Lange, R.A., and Hall, C.M. (2008) The eruptive history of the Mascota volcanic field, western Mexico: constraints on the origin of andesite among a diverse suite of lamprophyric and calc-alkaline lavas. Journal of Volcanology and Geothermal Research, 177, 1077-1091.

Parman, S.W., Dann, J.C., Grove, T.L., de Wit, M.J. (1997) Emplacement conditions of komatiite magmas from the 3.49Ga Komati Formation, Barberton Greenstone Belt, South Africa. Earth and Planetary Science Letters, 150, 303-323.

Pu, X., Lange, R.A. and Moore, G. (2017) A comparison of olivine-melt thermometers based on D_{Mg} and D_{Ni}: The effects of melt composition, temperature and pressure with applications to MORBs and hydrous arc basalts. American Mineralogist, 102, 750-765.

Putirka, K.D., Perfit, M., Ryerson, F.J., Jackson, M.G. (2007) Ambient and excess mantle temperatures, olivine thermometry, and active vs. passive upwelling. Chemical Geology, 241, 177-206.

Righter, K. and Carmichael, I.S.E. (1996) Phase equilibria of phlogopite lamprophyres from western Mexico: biotite-liquid equilibria and P-T estimates for biotite-bearing igneous rocks. Contributions to Mineralogy and Petrology, 123, 1-21.

Rosas-Elguera, J., Ferrari, L., Lopez-Martinez, M., Urrutia-Fucugauchi, J. (1997) Stratigraphy and tectonics of the Guadalajara region and the triple junction area, western Mexico. International Geological Review, 39, 125-140.

Sisson, T.W. and Grove, T.L. (1993a) Experimental investigations of the role of H_2O in calc-alkaline differentiation and subduction zone magmatism. Contributions to Mineralogist and Petrologist, 113,143-166.

Sisson, T.W. and Grove, T.L. (1993b) Temperatures and H_2O contents of low-MgO high-alumina basalts. Contributions to Mineralogist and Petrologist, 113, 167-184.

Wagner, T.P., Donnelly-Nolan, J.M., and Grove, T.L. (1995) Evidence of hydrous differentiation and crystal accumulation in the low-MgO, high-Al_2O_3 lake basalt from Medicine Lake volcano, California. Contributions to Mineralogy and Petrology, 121, 201-216.

Waters, L.E. and Lange, R.A. (2015) An updated calibration of the plagioclase-liquid hygrometer-thermometer applicable to basalts through rhyolites. American Mineralogist, 100, 2172-2184.

Waters, L.E., Andrews, B.J., Lange, R.A. (2015) Rapid crystallization of plagioclase phenocrysts in silicic melts during fluid-saturated ascent: phase equilibrium and decompression experiments. Journal of Petrology, 56, 981-1006.

Welsch, B., Hammer, J., Hellebrand, E. (2014) Phosphorus zoning reveals dentritic architecture of olivine. Geology, 42, 867-870.

Yang, T., Grand, S.P., Wilson, D., Guzman-Speziale, M., Gomez-Gonzalez, J.M., Dominguez-Reyes, T. and Ni, J. (2009) Seismic structure beneath the Rivera subduction zone from finite-frequency seismic tomography. Journal of Geophysical Research, 114, BO1302, doi:10.1029/2008JB005830

Zhang, Y., Xu, Z., Zhu, M., Wang, H. (2007). Silicate melt properties and volcanic eruptions. Reviews of Geophysics, 45, RG4004.

Figure Captions

Figure 1. Modified geologic map from Ownby et al., (2008). Numbered triangles in the Tepic-Zacoalco and Colima rifts refer to the central volcanoes: (1) V. Tequila, (2) V. Ceboruco, (3) V. Tepetiltic, (4) V. Sanganguey, (5) V. San Juan, (6) V. Colima, and (7) V. Tancítaro. The letters T, A, LV, and M refer to the towns of Tapalpa, Ayutla, Los Volcanes, and Mascota, respectively. The solid rectangle outlines the Mascota volcanic field, whereas the dashed square outlines the Michoacán-Guanajuato volcanic field (MGVF). Large cities are denoted by a black square.

Figures 2a and 2b. Modified sample map from Ownby et al., (2008). (a) Geologic sample map of the southern field area. (b) Geologic sample map of the northern field area.

Figure 3. Histograms of forsterite content of olivine phenocrysts from thirteen magmas from the Mascota volcanic field.

Figure 4. Plots of NiO wt% vs. Fo mol% for the most Mg-rich olivine analyses (highest 3 Fo mol% Fo) for 13 samples from the Mascota volcanic field. A linear fit to the data (equation in each plot) allows the NiO wt% to be calculated for the most forsteritic olivine analyzed in each sample.

Figure 5. Schematic diagram illustrating two competing hypotheses for where phenocryst growth occurs after melt segregation from its source region. One scenario (left) is that phenocryst growth occurs in a stalled magma chamber within the crust and eruption from this chamber occurs. Another scenario (right) is that phenocryst growth

occurs during ascent and there is no stalling of magma within a crustal chamber. If ascent is rapid enough, the composition of first olivine on the liquidus may be preserved and the whole-rock composition of the erupted ample can be used as a proxy for the liquid composition when the liquidus olivine crystallized.

Figure 6. Plot of calculated liquidus olivine composition from the MELTs thermodynamic model (Ghiroso and Sack 1995; Asimow and Ghiorso, 1998) based on the whole-rock composition vs. most Mg-rich olivine analyzed in each sample. MELTS calculations are run at four oxidation states: (ΔQFM = -1, 0, +1 and +2). The results show that over these reasonable redox conditions, the hypothesis of phenocryst during ascent, where the most Mg-rich olivine in each thin section approximate the liquidus olivine and where the whole-rock composition approximates the liquid composition from which all phenocrysts grew, is viable.

Figure 7. Back-scattered electron (BSE) images that show diffusion-limited growth textures of olivine phenocryst in 10 of 13 lavas erupted from the Mascota volcanic field.

Figure 8. Simplified phase diagram based off of the phase-equilibrium experiments by Moore and Carmichael (1998) on a basaltic andesite (Mas-22) under pure-H_2O fluid-saturated conditions. Abbreviations of mineral phases: Hbl (hornblende); Ol (olivine); Pl (plagioclase); Aug (augite). The dashed lines are isopleths of maximum H_2O solubility in the melt from the model in Zhang et al. (2007). A plausible adiabatic ascent path (arrow) is shown for Mas-19 (intersects olivine-in curve at 1072 °C based on Ni-thermometry results; Table 1), which has a bulk composition similar to that for MAS-22. Also shown

is a plausible adiabatic ascent path of a hornblende-lamprophyre (Mas-9), which intersects the olivine liquidus at 954ºC.

Figure 9a and 9b. (a) Comparison of Fe^{3+}/Fe^{T} (K_D=.37) between six basaltic andesites from Mascota (blue) and 17 basaltic andesites from the Michoacán-Guanajuato volcanic field (gray) from Pu et al., (2017). (b) Comparison of ΔT (= $T_{Mg} - T_{Ni}$) between six basaltic andesites from Mascota (blue) and 17 basaltic andesites from the Michoacán-Guanajuato volcanic field (gray) from Pu et al., (2017).

Table 1. Whole-rock compositions and olivine-melt thermometry results

	LV-134	MAS-48	MAS-102	MAS-11	MAS-3	MAS-198
	Absarokite	Absarokite	Absarokite	Olivine Minette	Olivine Minette	Olivine Minette
Whole-Rock Composition						
SiO_2	49.3	50.0	50.3	51.1	51.1	52.2
TiO_2	1.20	1.84	1.01	1.88	1.87	1.55
Al_2O_3	12.1	12.5	15.1	13.3	13.2	16.3
FeO^T	8.05	7.69	7.77	7.18	7.09	6.40
MnO	0.12	0.13	0.12	0.14	0.14	0.13
MgO	16.8	12.0	11.8	9.0	8.8	6.8
CaO	7.4	8.4	8.4	7.7	7.6	8.9
Na_2O	2.44	2.82	3.59	2.59	2.77	3.35
K_2O	1.95	3.64	1.42	5.67	5.84	3.55
P_2O_5	0.56	1.04	0.45	1.51	1.50	0.74
Ni (ppm)	371	412	241	300	296	102
Total	99.30	100.40	99.55	99.93	99.55	100.34
Calculated temperature and minimum H_2O						
Max Fo Content	91.4	92.4	89.5	90.2	89.6	89.4
$D_{Mg}^{ol/liq}$	2.7	3.7	3.8	4.7	4.8	6.1
T_{Mg} ºC	1404	1329	1313	1279	1279	1199
Olivine NiO (wt%)	0.58	0.69	0.38	0.77	0.72	0.37
$D_{Ni}^{ol/liq}$	12.2	13.3	12.4	20.1	19.2	28.5
T_{Ni} ºC	1193	1202	1218	1140	1152	1088
ΔT	211	127	95	139	127	112
Min H_2O wt%	8.5	3.9	2.6	4.5	4.0	3.3
Calculated Fe^{3+}/Fe^T and ΔNNO						
Fe^{3+}/Fe^T (K_D=.37)	0.05	0.34	0.13	0.35	0.30	0.39
ΔNNO (K_D =.37)	-3.5	1.8	-1.0	1.4	0.9	1.8

See Carmichael et al. (1996) and Lange and Carmichael (1991) for details on analytical methods and results. T_{Mg} and T_{Ni} are from olivine-melt thermometers from Pu et al. (2017). K_D of 0.37 is based on a compilation of hydrous experiments evaluated in Pu et al. (2017). Calculation of oxygen fugacity (and thus ΔNNO) is from Eq. 12 in from the model of Jayasuriya et al. (2004).

Table 1 continued. Whole-rock compositions and olivine-melt thermometry results

	MAS-149	MAS-42	MAS-21	MAS-45	MAS-41	MAS-19	MAS-9
	Basaltic Andesite	Basaltic Andesite	Basaltic Andesite	Basaltic Andesite	Basaltic Andesite	Basaltic Andesite	Hornblende Lamprohyre
Whole-Rock Composition							
SiO_2	54.8	54.0	53.6	53.1	55.1	56.5	52.8
TiO_2	0.72	0.87	0.83	0.91	0.77	0.73	1.27
Al_2O_3	16.9	16.8	16.9	17.4	17.6	17.7	16.7
FeO^T	6.52	6.92	6.54	6.84	6.22	6.18	6.84
MnO	0.12	0.12	0.12	0.12	0.12	0.12	0.13
MgO	8.7	8.4	8.1	7.8	7.1	6.1	6.2
CaO	7.3	7.9	8.5	8.6	7.8	7.1	8.3
Na_2O	3.89	3.82	4.12	4.20	3.99	4.21	3.85
K_2O	0.88	0.99	1.02	0.87	1.08	1.03	3.09
P_2O_5	0.20	0.13	0.28	0.17	0.26	0.31	0.74
Ni (ppm)	113	134	120	120	130	124	65
Total	100.48	100.26	100.19	99.94	99.93	99.77	99.49
Calculated temperature and minimum H_2O							
Max Fo Content	88.8	92.4	89.4	88.6	88.9	86.2	88.1
$D_{Mg}^{ol/liq}$	5.0	5.1	5.3	5.5	6.0	6.8	6.6
T_{Mg} ºC	1246	1235	1227	1217	1204	1181	1188
Olivine NiO (wt%)	0.54	0.66	0.42	0.40	0.55	0.58	0.54
$D_{Ni}^{ol/liq}$	37.7	38.2	27.8	25.6	33.4	35.5	65.6
T_{Ni} ºC	1038	1031	1090	1102	1069	1068	954
ΔT	207	204	137	115	135	114	234
Min H_2O wt%	8.3	8.0	4.4	3.4	4.3	3.2	10.0
Calculated Fe^{3+}/Fe^T and ΔNNO							
Fe^{3+}/Fe^T (K_D=.37)	0.19	0.49	0.29	0.26	0.30	0.25	0.41
ΔNNO (K_D =.37)	0.0	3.0	1.1	0.7	1.2	0.6	1.9

See Carmichael et al. (1996) and Lange and Carmichael (1991) for details on analytical methods and results. TMg and TNi are from olivine-melt thermometers from Pu et al. (2017). KD of 0.37 is based on a compilation of hydrous experiments evaluated in Pu et al. (2017). Calculation of oxygen fugacity (and thus ΔNNO) is from Eq. 12 in from the model of Jayasuriya et al. (2004).

Table 2. Analyses of most Mg-rich olivine in each sample

	LV-134	MAS-102	MAS-48	MAS-11	MAS-3	MAS-198
	Absarokite	Absarokite	Absarokite	Olivine Minette	Olivine Minette	Olivine Minette
SiO_2 (wt%)	41.80	41.30	41.74	41.39	40.67	41.07
TiO_2 (wt%)	0.00	0.00	0.00	0.00	0.00	0.00
Al_2O_3 (wt%)	0.03	0.01	0.02	0.01	0.01	0.03
Cr_2O_3 (wt%)	0.07	0.02	0.08	0.10	0.07	0.01
NiO (wt%)	0.58	0.41	0.67	0.56	0.75	0.38
FeO^T (wt%)	8.30	9.98	7.33	9.41	9.94	9.99
MnO (wt%)	0.09	0.11	0.07	0.10	0.16	0.15
MgO (wt%)	49.19	47.48	49.68	48.38	47.80	47.25
CaO (wt%)	0.13	0.13	0.13	0.13	0.11	0.17
Total	100.20	99.44	99.72	100.07	99.50	99.05
all Fe^{2+} and O = 4						
Si	1.02	1.02	1.02	1.01	1.01	1.02
Ti	0.00	0.00	0.00	0.00	0.00	0.00
Al	0.00	0.00	0.00	0.00	0.00	0.00
Cr	0.00	0.00	0.00	0.00	0.00	0.00
Ni	0.01	0.01	0.01	0.01	0.01	0.01
Fe	0.17	0.21	0.15	0.19	0.21	0.21
Mn	0.00	0.00	0.00	0.00	0.00	0.00
Mg	1.78	1.74	1.80	1.76	1.76	1.74
Ca	0.00	0.00	0.00	0.00	0.00	0.00
$\sum$ cations	2.98	2.98	2.98	2.99	2.99	2.98
% Fa	8.60	10.5	7.6	9.8	10.5	10.6
% Fo	91.4	89.5	92.4	90.2	89.5	89.4

Table 2 continued. Analyses of most Mg-rich olivine in each sample

	MAS-149	MAS-42	MAS-21	MAS-45	MAS-41	MAS-19	MAS-9
	Basaltic Andesite	Basaltic Andesite	Basaltic Andesite	Basaltic Andesite	Basaltic Andesite	Basaltic Andesite	Hornblende Lamprophyre
SiO_2 (wt%)	40.75	41.35	41.68	41.33	40.80	40.99	41.16
TiO_2 (wt%)	0.00	0.00	0.00	0.00	0.00	0.00	0.00
Al_2O_3 (wt%)	0.03	0.02	0.02	0.02	0.02	0.01	0.01
Cr_2O_3 (wt%)	0.09	0.10	0.02	0.02	0.06	0.05	0.05
NiO (wt%)	0.60	0.64	0.38	0.36	0.57	0.48	0.59
FeO^T (wt%)	10.55	7.26	10.10	10.95	10.50	13.04	11.29
MnO (wt%)	0.13	0.08	0.15	0.22	0.09	0.22	0.19
MgO (wt%)	46.97	49.55	47.57	47.66	47.04	45.48	47.07
CaO (wt%)	0.09	0.14	0.10	0.10	0.10	0.10	0.10
Total	99.21	99.13	100.02	100.66	99.18	100.36	100.47
all Fe^{2+} and O = 4							
Si	1.01	1.01	1.02	1.01	1.01	1.02	1.01
Ti	0.00	0.00	0.00	0.00	0.00	0.00	0.00
Al	0.00	0.00	0.00	0.00	0.00	0.00	0.00
Cr	0.00	0.00	0.00	0.00	0.00	0.00	0.00
Ni	0.01	0.01	0.01	0.01	0.01	0.01	0.01
Fe	0.22	0.15	0.21	0.22	0.22	0.27	0.23
Mn	0.00	0.00	0.00	0.00	0.00	0.00	0.00
Mg	1.74	1.81	1.74	1.74	1.74	1.68	1.73
Ca	0.00	0.00	0.00	0.00	0.00	0.00	0.00
∑ cations	2.99	2.99	2.98	2.99	2.99	2.98	2.99
% Fa	11.2	7.6	10.6	11.4	11.1	13.9	11.9
% Fo	88.8	92.4	89.4	88.6	88.9	86.1	88.1

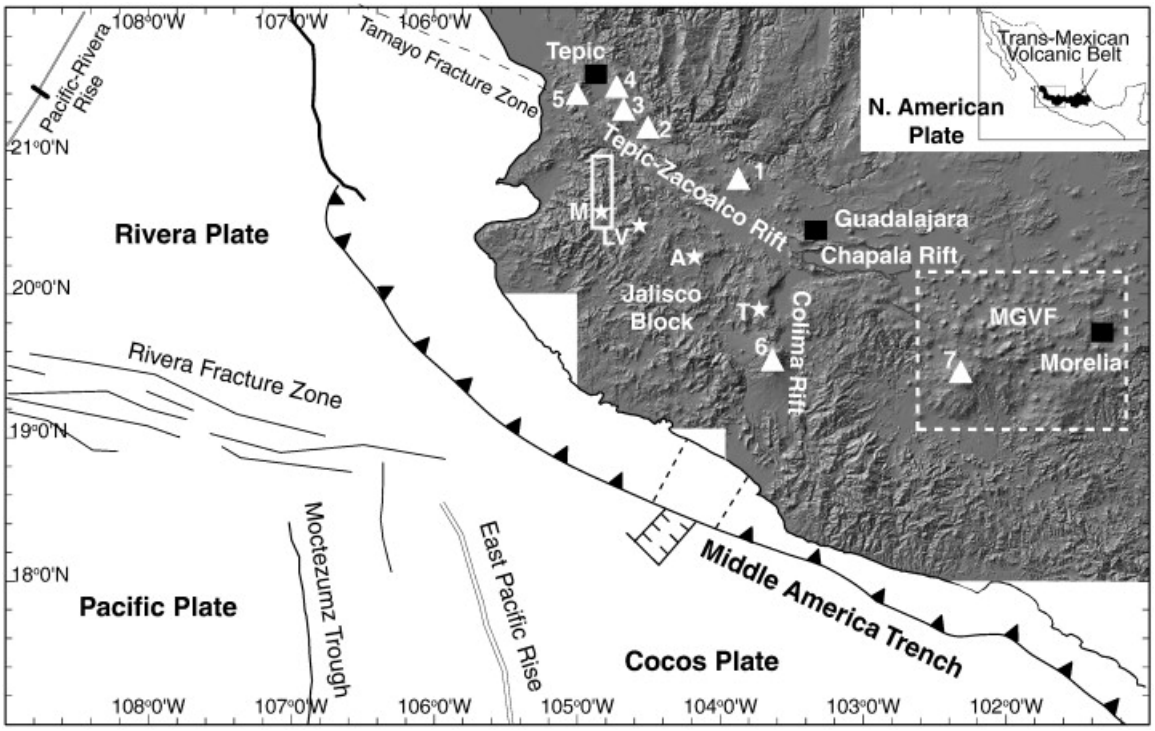
108°0'W
107°0'W
106°0'W
Tamayo Fracture Zone
Pacific-Rivera Rise
21°0'N
20°0'N
19°0'N
18°0'N
Tepic
4
5
3
2
1
Tepic-Zacoalco Rift
M
LV
A
Guadalajara
Chapala Rift
Rivera Plate
Jalisco Block
T
Colima Rift
6
MGVF
7
Morelia
Rivera Fracture Zone
Moctezumz Trough
East Pacific Rise
Middle America Trench
Pacific Plate
Cocos Plate
105°0'W
104°0'W
103°0'W
102°0'W
N. American Plate
Trans-Mexican Volcanic Belt

Figure 1

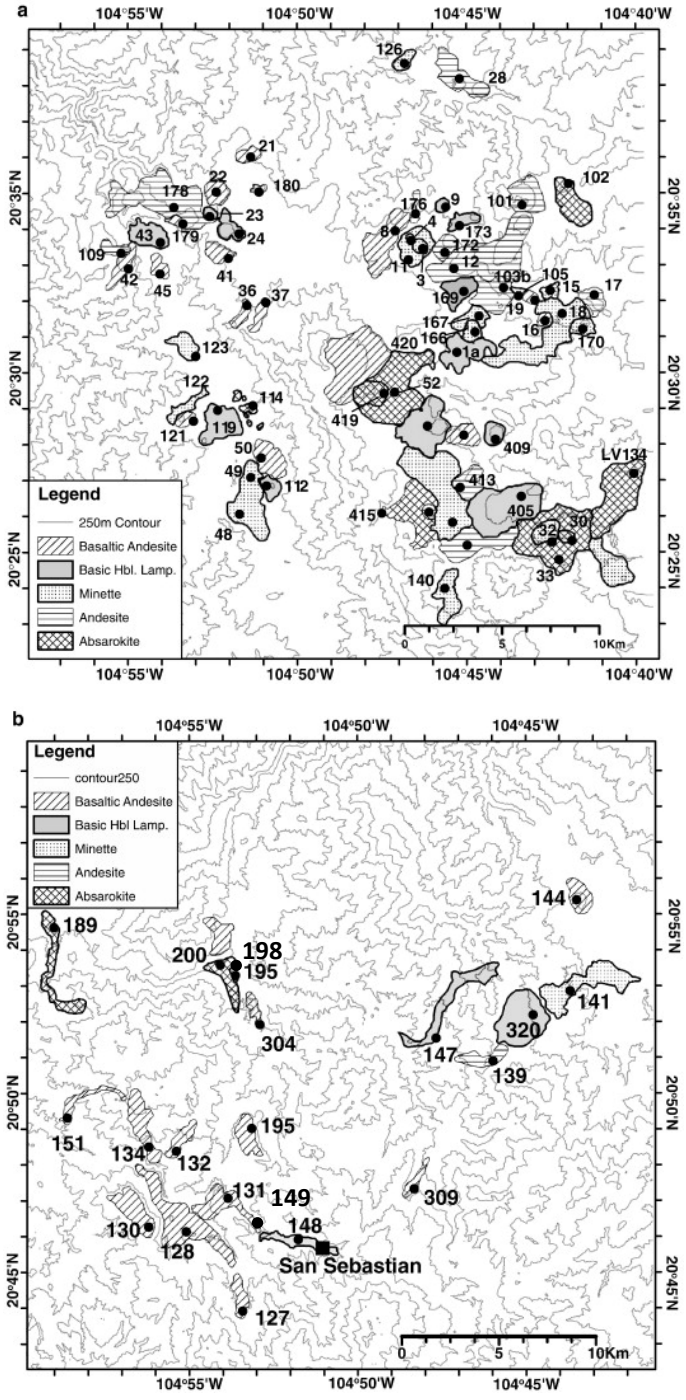

Figure 2 (a and b)

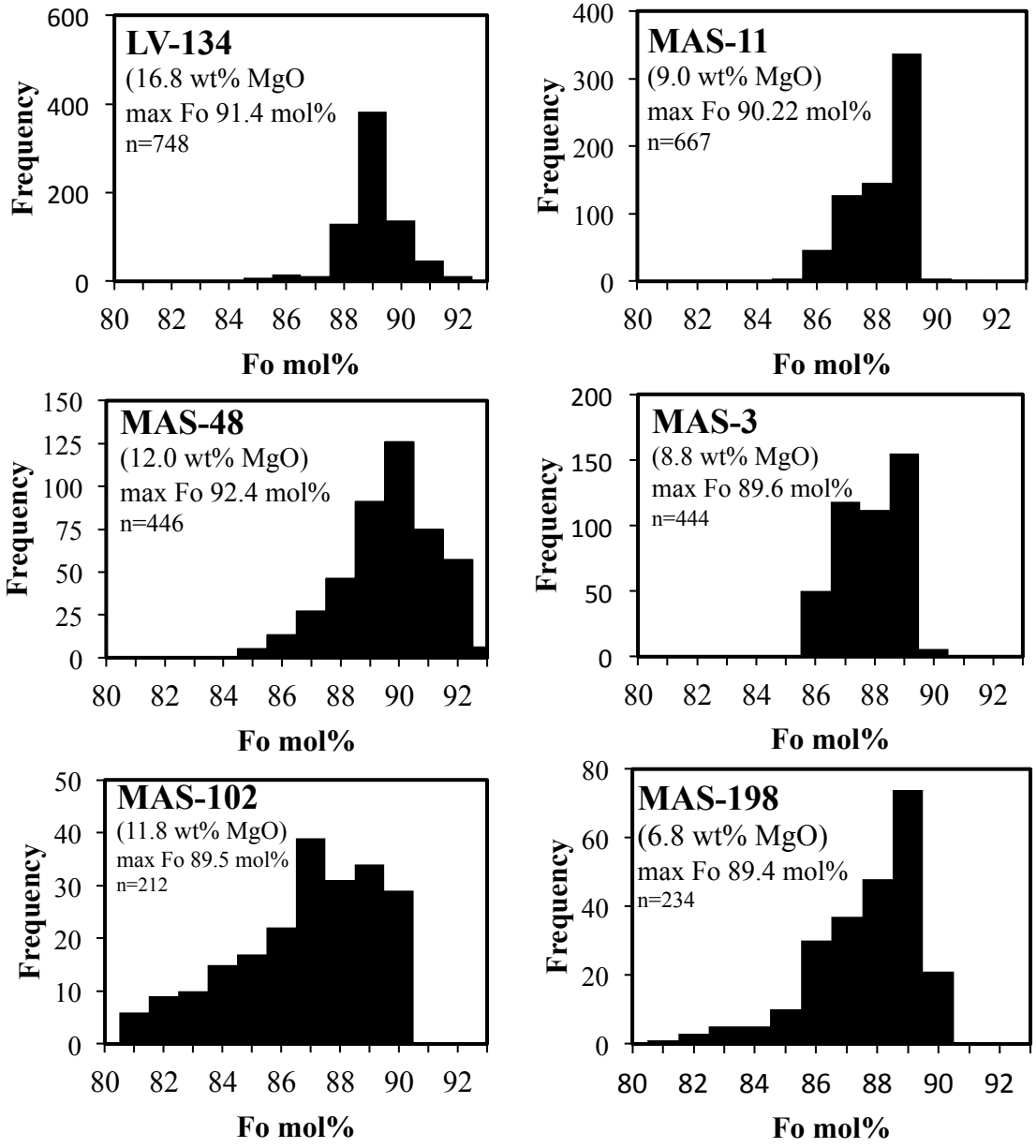
LV-134
(16.8 wt% MgO
max Fo 91.4 mol%
n=748
MAS-11
(9.0 wt% MgO)
max Fo 90.22 mol%
n=667
MAS-48
(12.0 wt% MgO)
max Fo 92.4 mol%
n=446
MAS-3
(8.8 wt% MgO)
max Fo 89.6 mol%
n=444
MAS-102
(11.8 wt% MgO)
max Fo 89.5 mol%
n=212
MAS-198
(6.8 wt% MgO)
max Fo 89.4 mol%
n=234
Frequency
Fo mol%

Figure 3

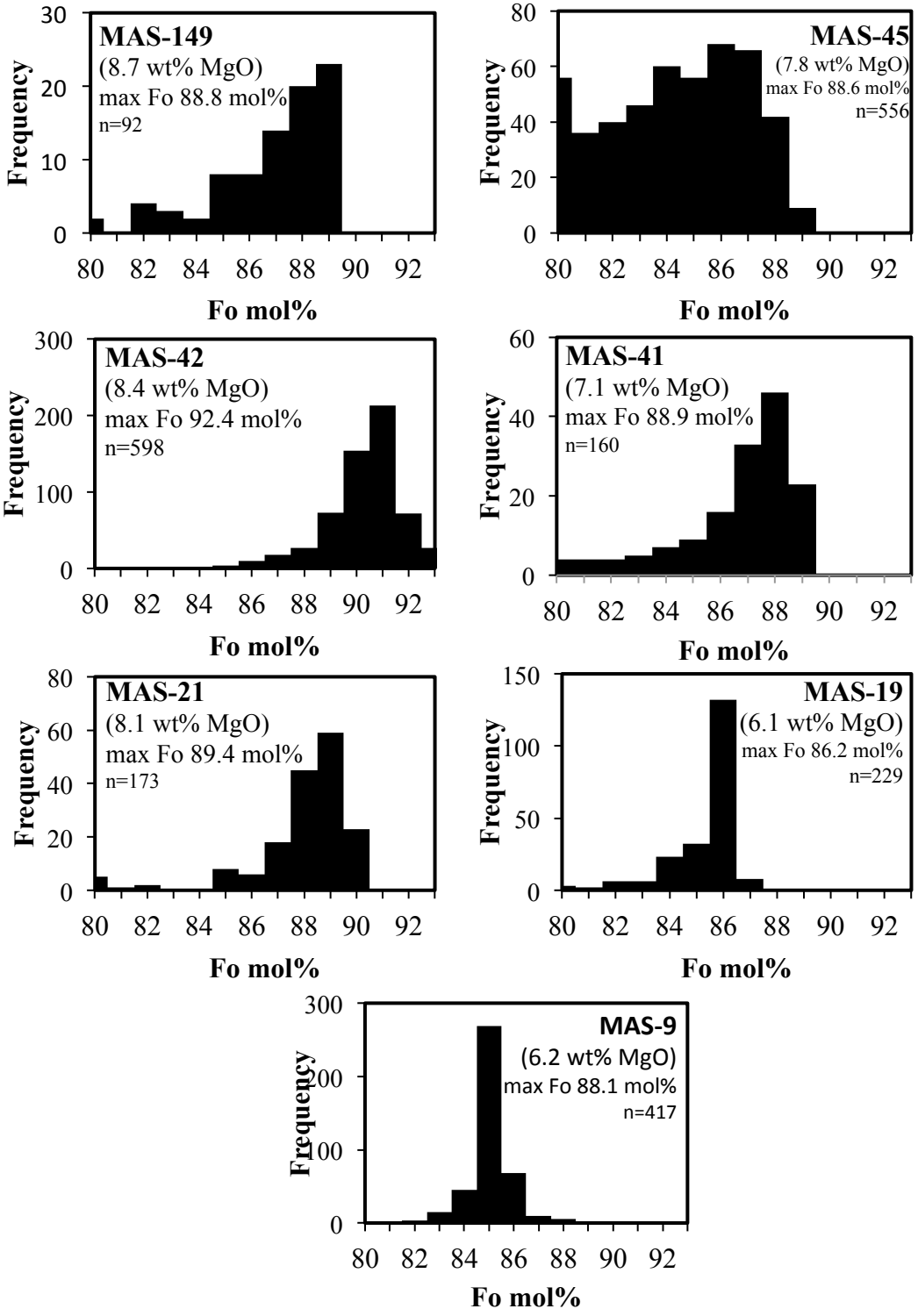

Figure 3 cont.

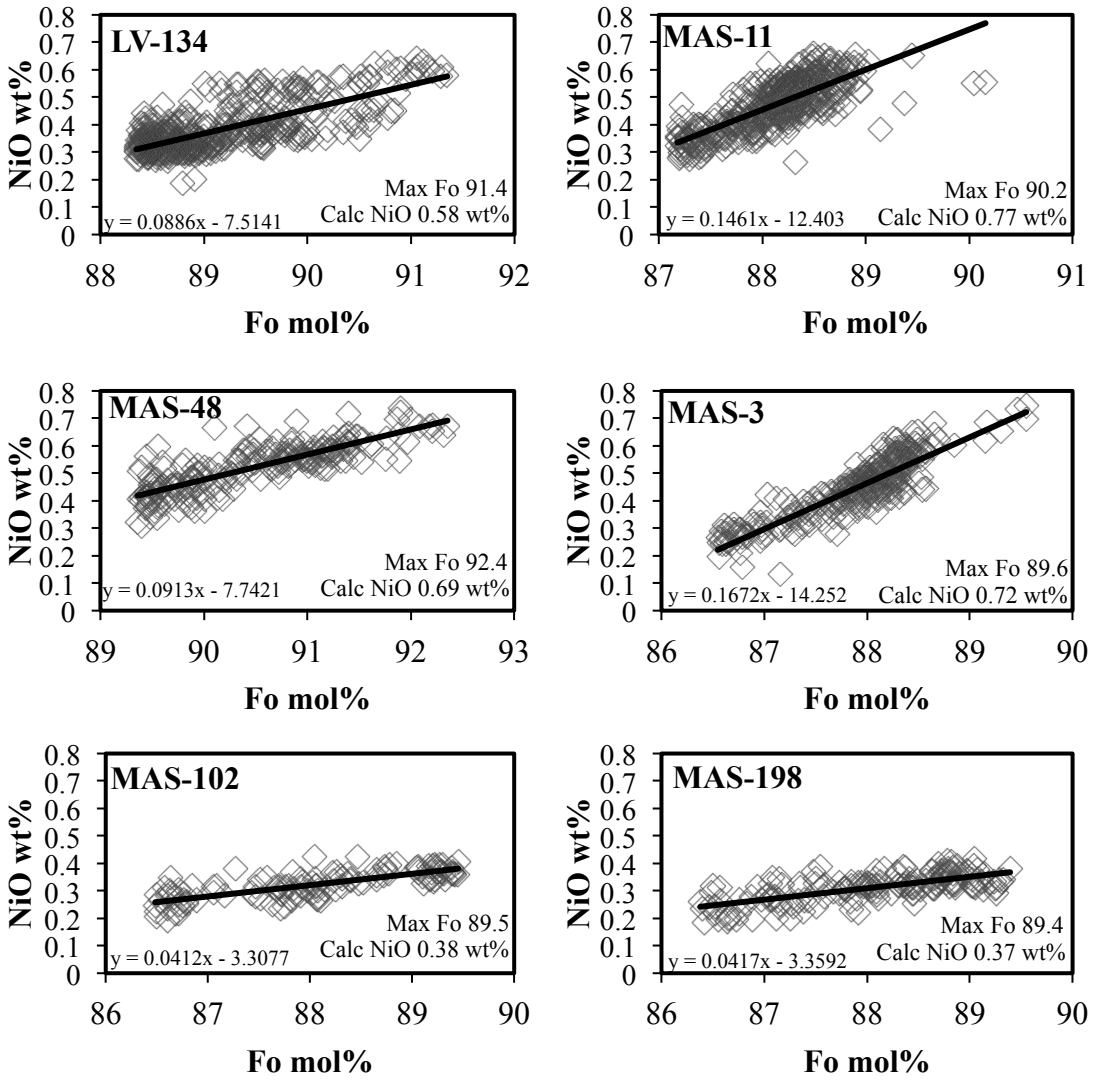
LV-134
y = 0.0886x - 7.5141
Max Fo 91.4
Calc NiO 0.58 wt%
MAS-11
y = 0.1461x - 12.403
Max Fo 90.2
Calc NiO 0.77 wt%
MAS-48
y = 0.0913x - 7.7421
Max Fo 92.4
Calc NiO 0.69 wt%
MAS-3
y = 0.1672x - 14.252
Max Fo 89.6
Calc NiO 0.72 wt%
MAS-102
y = 0.0412x - 3.3077
Max Fo 89.5
Calc NiO 0.38 wt%
MAS-198
y = 0.0417x - 3.3592
Max Fo 89.4
Calc NiO 0.37 wt%
NiO wt%
Fo mol%

Figure 4

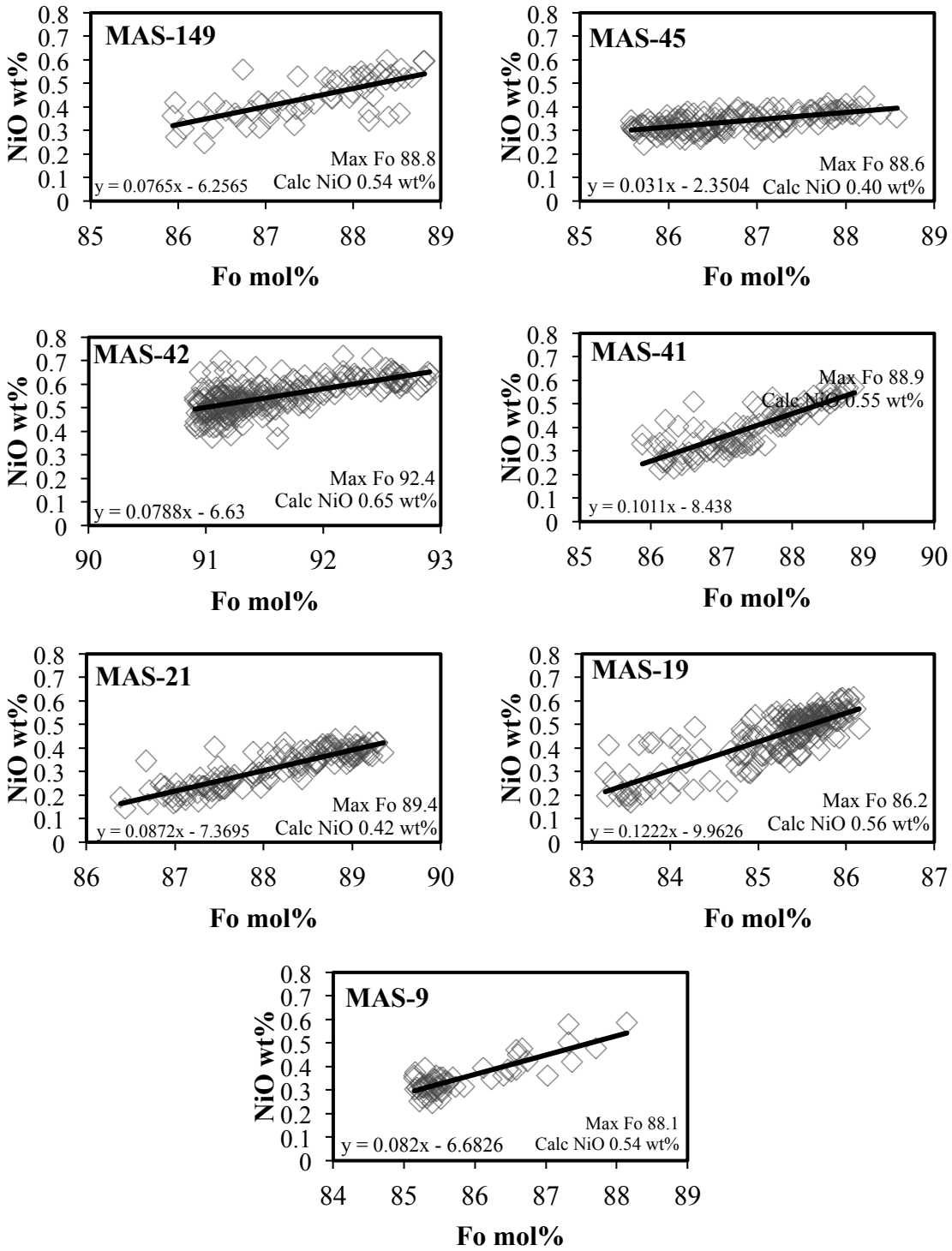

Figure 4 cont.

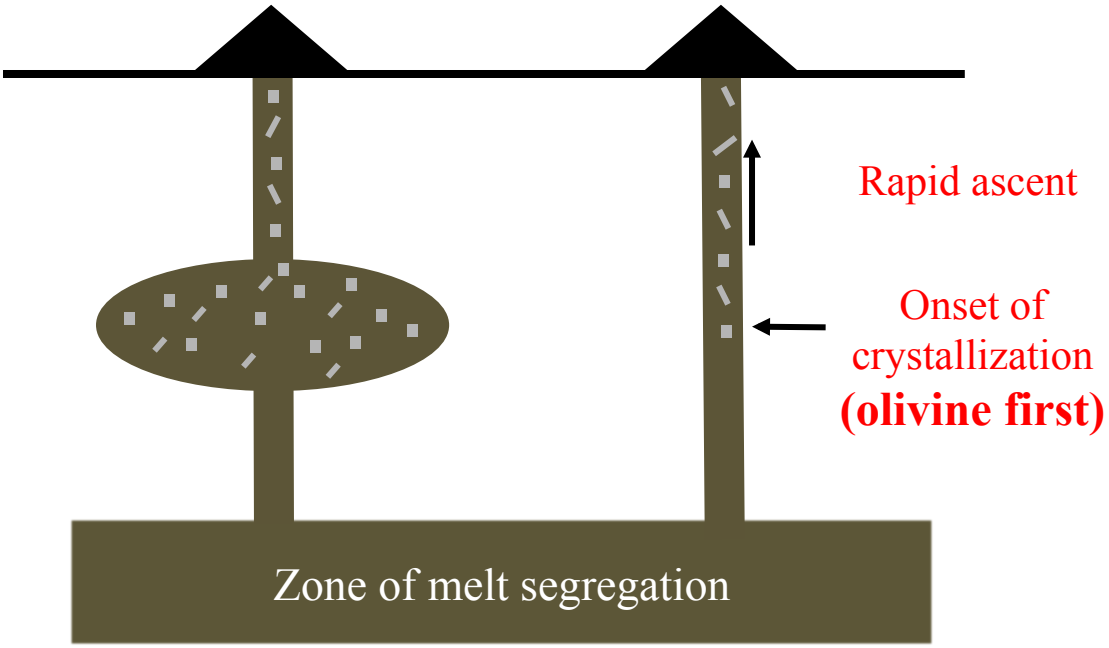
Rapid ascent
Onset of
crystallization
(olivine first)
Zone of melt segregation

Figure 5

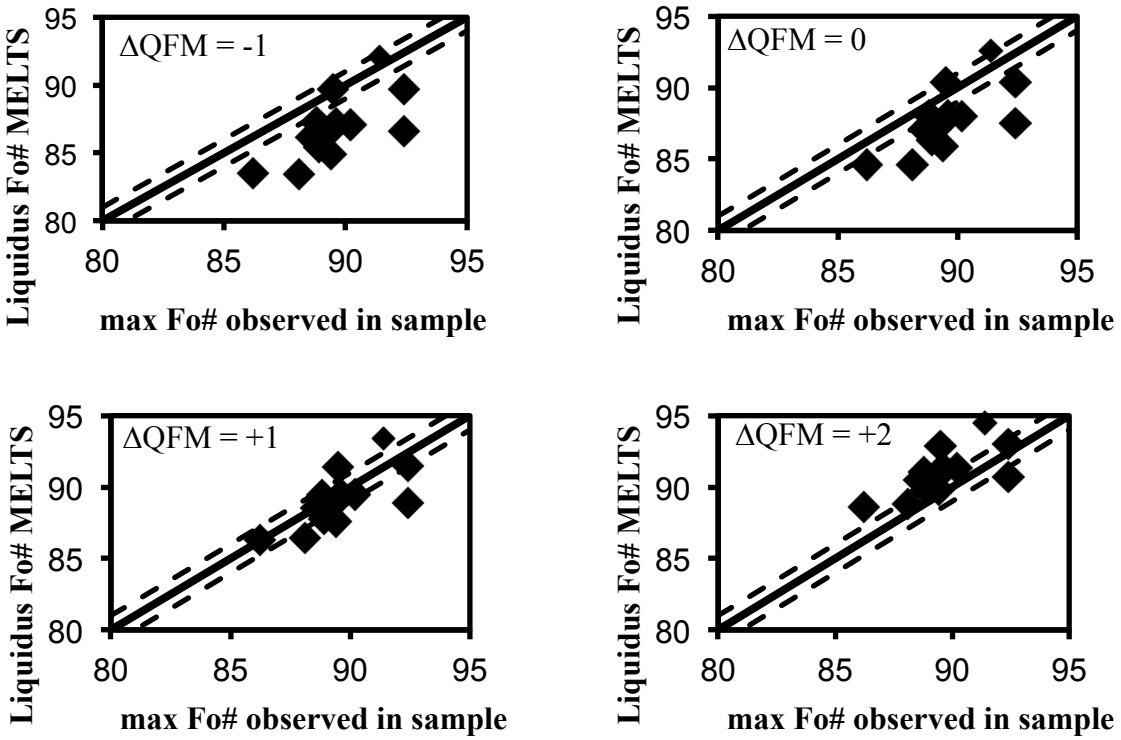
ΔQFM = -1
ΔQFM = 0
ΔQFM = +1
ΔQFM = +2
Liquidus Fo# MELTS
max Fo# observed in sample
80
85
90
95

Figure 6

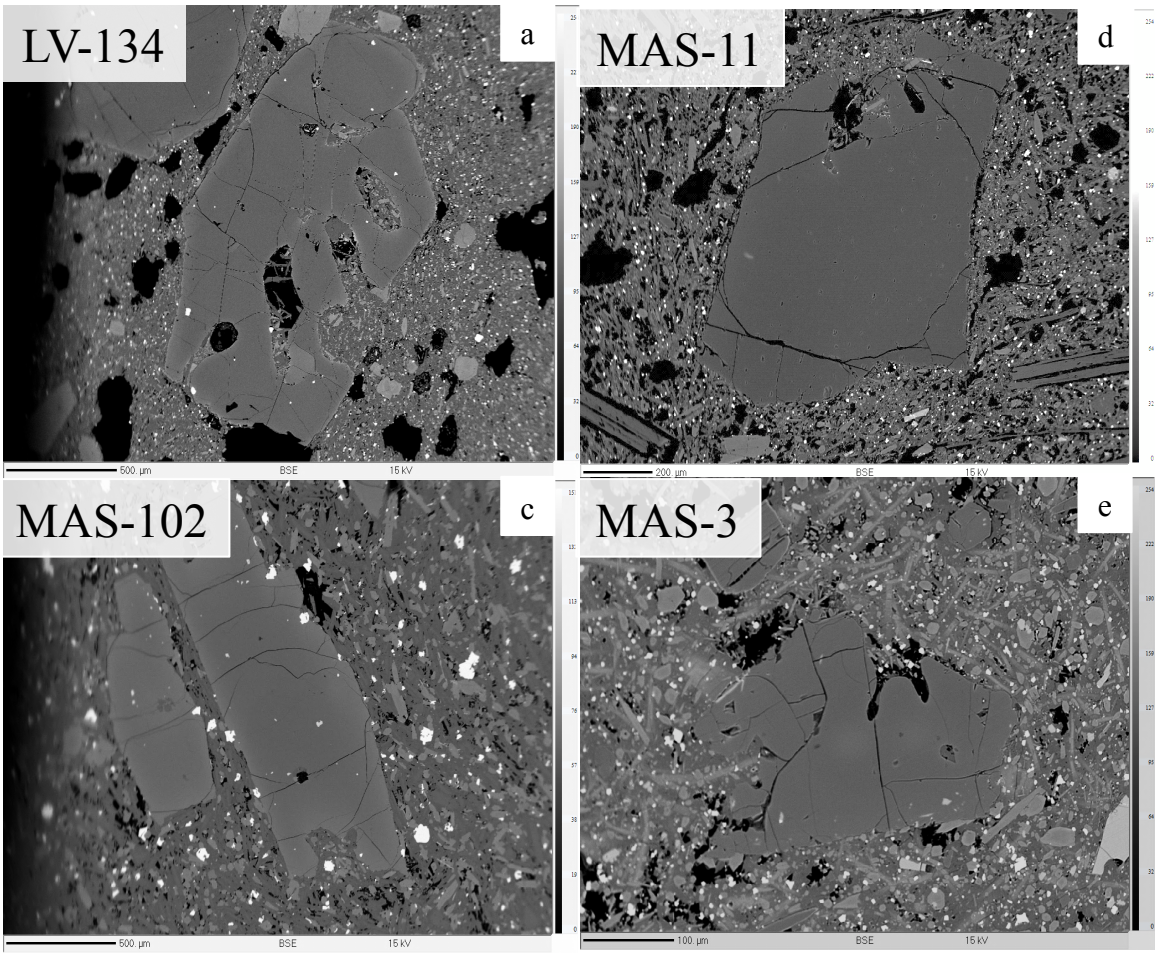
LV-134
a
500. µm
BSE
15 kV
MAS-11
d
200. µm
BSE
15 kV
MAS-102
c
500. µm
BSE
15 kV
MAS-3
e
100. µm
BSE
15 kV

Figure 7

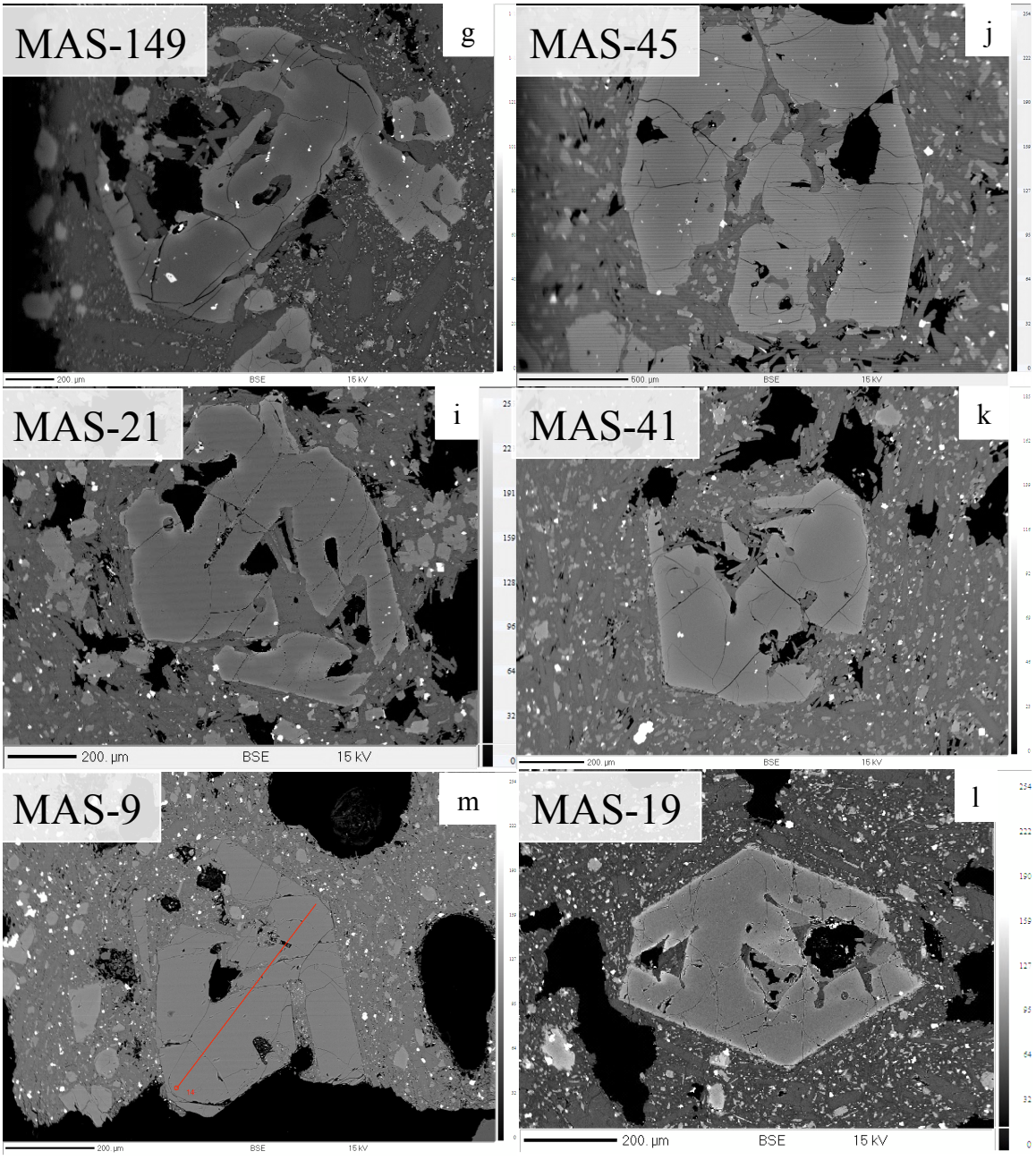

Figure 7 cont.

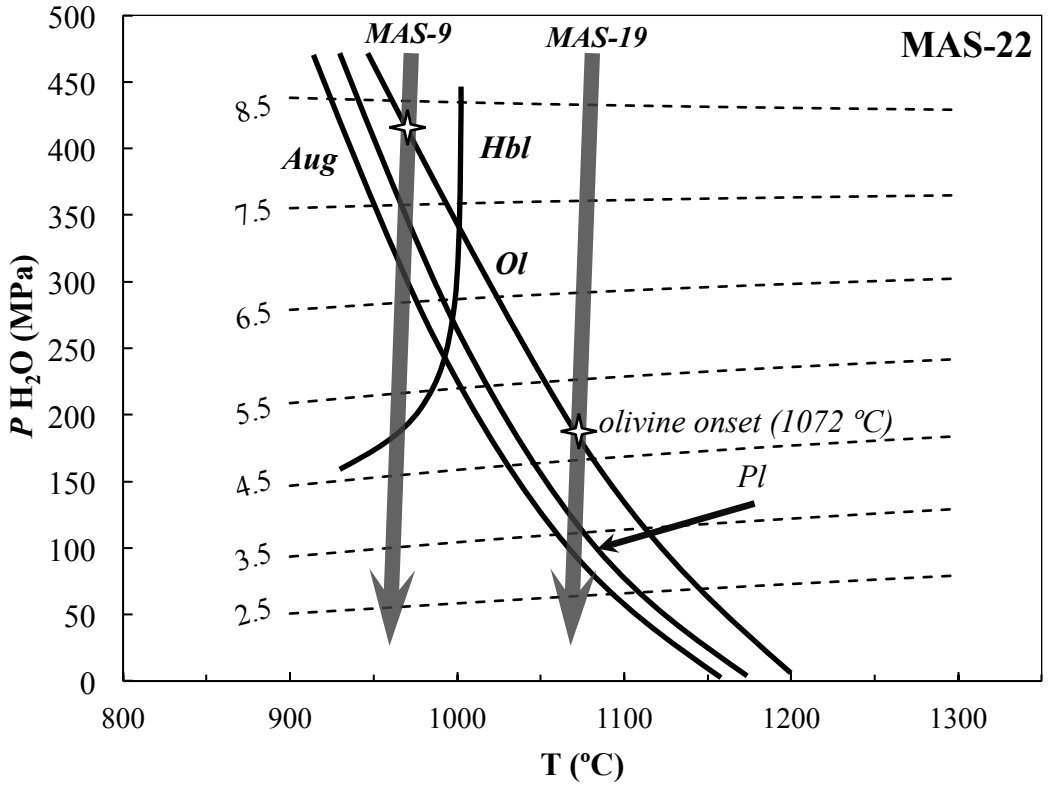
MAS-9
MAS-19
MAS-22
Aug
Hbl
Ol
Pl
olivine onset (1072 ºC)
8.5
7.5
6.5
5.5
4.5
3.5
2.5
P H2O (MPa)
T (ºC)
500
450
400
350
300
250
200
150
100
50
0
800
900
1000
1100
1200
1300

Figure 8

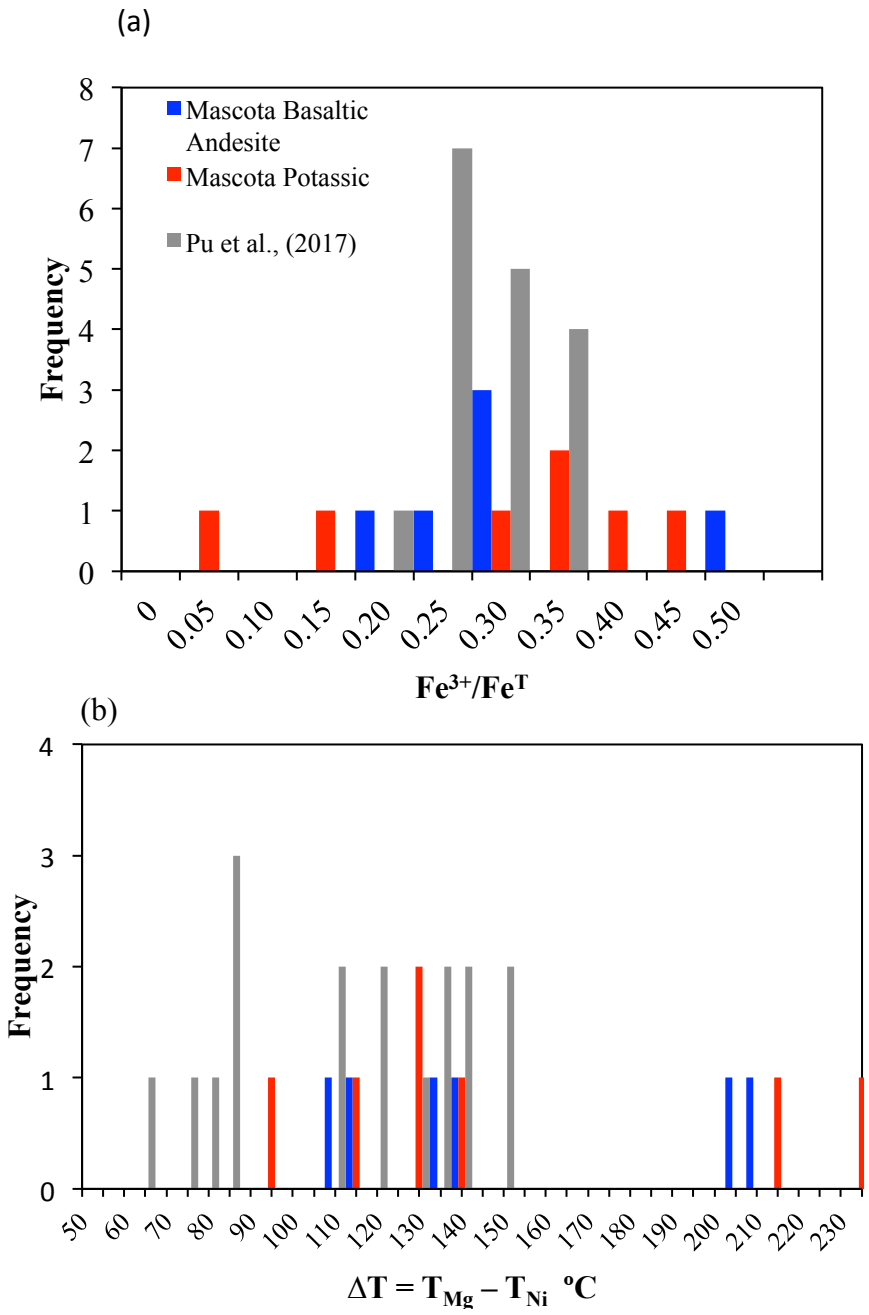

Figure 9 (a and b)